

System Frequency Nadir and Trajectory Prediction with Discontinuity Constraints in Governor Dynamics

Jongoh Baek, *Student Member, IEEE*, Luke Lowery, *Student Member, IEEE*,
and Adam B. Birchfield, *Senior Member, IEEE*

Abstract— Accurately predicting the frequency nadir and estimating the overall frequency trajectory are crucial analytical tasks in power system planning. Given the large number of operating scenarios and contingency events that must be evaluated, low-order frequency nadir prediction (FNP) models have been recently developed to avoid the computational burden of full dynamic simulations in large, complex systems. However, a major technical limitation of existing FNP models is their inability to capture inherent discontinuities such as limits, piecewise functions, and deadbands that strongly influence the actual frequency dynamics. To overcome these challenges, this paper proposes a discontinuity-aware frequency nadir prediction (DA-FNP) model that explicitly implements discontinuity constraints into the frequency response estimation. By implementing these discontinuities, the model not only predicts the system frequency trajectory with high fidelity but also identifies which generators are subject to enforced constraints. This capability provides new insights for system planners, enabling a more realistic evaluation of frequency security margins and resource adequacy in future power systems with high renewable penetration. The methodology is validated against detailed dynamic simulations on both small- and large-scale synthetic grids. The case study demonstrates significant enhancement on the accuracy of system configuration and system frequency trajectory, while retaining computational efficiency of low-order models. Furthermore, the approach offers a practical and scalable tool for planning studies in large, complex power systems.

Index Terms— Frequency nadir prediction (FNP) model, discontinuity-awareness, turbine-governor dynamics, and system frequency response trajectory.

I. INTRODUCTION

The transition toward low-inertia, renewable-dominated power systems poses substantial challenges to grid stability, especially under disturbance events. The reduced overall system inertia from increased penetration of Inverter-Based Resources (IBRs) accelerates the Rate of Change of Frequency (RoCoF) during inertial response, weakening the primary frequency response (PFR) and causing lower frequency nadir [1], [2]. A lower frequency nadir potentially triggers the underfrequency load shedding (UFLS) programs to arrest frequency decline and stabilize the grid during severe

disturbances [3], [4]. While UFLS is an essential protective mechanism to prevent system-wide blackouts, it disrupts power supply to end-users, raising reliability concerns. For example, during the severe winter storm of 2021 in Texas, millions of customers experienced prolonged outages, though the grid operator implemented manual load shedding prior to activating UFLS scheme to mitigate further instability [5]. In some cases, UFLS alone is insufficient, as seen in the 2016 South Australia blackout, where rapid frequency decline prevented UFLS activation [6]. These events highlight the need for accurate prediction of the frequency nadir and the overall frequency trajectory to enable engineers to identify risks for frequency instability and identify corrective actions, reducing reliance on UFLS and enhancing grid resilience. While traditional full dynamic simulations are highly accurate for frequency response prediction, these simulations are computationally intensive and time-consuming, especially for large power systems with complex models. This highlights the need for faster, more efficient frequency estimation methods. Consequently, low-order modeling frameworks have been developed to consider the large number of operating scenarios and contingency events.

Early efforts to predict frequency trajectory and nadir focused on modeling average system frequency (ASF) and low-order system frequency response (SFR) behavior based on governor actions and system characteristics, while neglecting system topology and inter-machine oscillations [7], [8]. Researchers have since adapted the ASF and SFR models to modern power systems with diverse governors and prime movers, though they may not fully capture system complexity [9]–[21]. One adaptation introduced an open-loop, aggregated first-order model for governors and prime movers, validated on small, isolated power systems in Spain [13]. For frequency nadir prediction (FNP) model in large-scale power systems, another approach proposed an analytical method using polynomial fitting of each governor’s unit step response, eliminating reliance on detailed network models [14]. With increasing the IBR integration, new methods are essential for incorporating the IBR dynamics into ASF frameworks. A generic ASF (G-ASF) model was developed, integrating IBRs

This material is based upon work supported in part by the National Science Foundation under Grant No. 2442131.

The authors are with the Department of Electrical and Computer Engineering, Texas A&M University, College Station, TX 77843 USA (email: jongoh@tamu.edu; lukel@tamu.edu; abirchfield@tamu.edu).

with virtual inertia and hydro governors, along with an online inertia allocation strategy [15]. Further advancements have considered frequency-voltage interactions by incorporating generator excitation control and power system stabilizers for a more realistic grid representation [16]. A general-order SFR model incorporating fixed and adaptive UFLS schemes was also proposed to improve estimation accuracy [17]. Additionally, governor deadband effects on frequency nadir have been captured using a describing function approach [18]. Despite these advancements, previous models assume constant governor output after disturbances and fail to account for major discontinuities, such as inherent turbine-governor limits. Beyond analytical methods, data-driven modeling techniques have been explored for predicting maximum frequency deviation including artificial neural networks [22]-[26]. While these methods offer advantages in pattern recognition and adaptability, they may be less effective in certain non-stationary scenarios.

A major limitation of existing frequency nadir prediction (FNP) models is their inability to accurately reproduce the frequency response obtained from detailed dynamic simulations of large-scale power systems. This gap arises because conventional approaches neglect the discontinuity constraints inherent in practical governor models, which can significantly influence the actual frequency nadir following a disturbance. To overcome this issue, this paper proposes a discontinuity-aware frequency nadir prediction (DA-FNP) model that explicitly implements these discontinuities, thereby improving the accuracy of system frequency response estimation across a wide range of operating conditions and contingencies. To the best of our knowledge, this aspect has not been systematically addressed in existing literature. The proposed framework considers the following features:

- frequency deadbands, which prevent unnecessary governor actions due to measurement noise but delay frequency recovery;
- physical constraints, such as valve limits in turbine-governor systems, commonly represented by limiter blocks in detailed dynamic models; and
- logical constraints, reflecting control strategies designed to balance stability and efficiency.

By implementing these discontinuities, the DA-FNP model not only predicts the system frequency trajectory with high fidelity but also identifies which generators are subject to enforced constraints. This capability provides new insights for system planners, enabling a more realistic evaluation of frequency security margins and resource adequacy in future power systems with high renewable penetration. The effectiveness of the proposed method is validated against full dynamic simulations for both small- and large-scale systems, including the Hawaii (37-bus, 30-generator) and Texas (2000-bus, 313-generator) synthetic grids. Results demonstrate that the proposed model achieves both analytical accuracy and computational efficiency, thereby offering a practical and scalable tool for planning studies in large, complex power grids.

This paper is structured as follows: Section II describes the analytical background for FNP model. Section III describes the methodology for implementing discontinuity constraints to the FNP model. Section IV presents the proposed algorithm for newly formulated DA-FNP model. Section V provides a case study validating the proposed method. Finally, Section VI concludes this paper.

II. BACKGROUND: CORE ANALYTICAL MODEL FOR FREQUENCY NADIR PREDICTION

This section presents the analytical background for estimating the system frequency trajectory under fundamental conditions, without incorporating any discontinuity constraints.

A recent analytical framework for FNP model employs an open-loop formulation with parabolic frequency deviation as input [14]. This approach decouples the calculation of turbine-governor response from frequency deviation, as illustrated in Fig. 1.

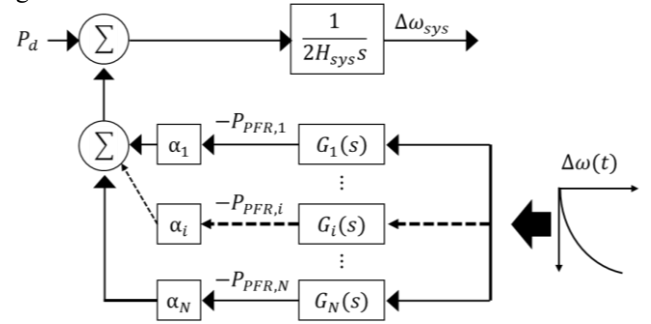


Fig. 1. Open-loop for frequency nadir prediction model.

The frequency nadir is reached when the mechanical power output equals the electrical power demand after a disturbance, i.e., when the aggregated PFR power, $P_{PFR,sys}$ matches the load power imbalance. Before reaching the frequency nadir, the dynamic behavior of the $P_{PFR,sys}$ can be approximated by (1), as a linear ramp with constant slope.

$$P_{PFR,sys}(t) = \frac{P_d}{t_n} t, t \in [0, t_n] \quad (1)$$

where P_d is the power deficit and t_n is the time when the frequency nadir occurs under a positive P_d event. In the open-loop formulation, the equivalent system-wide frequency deviation is represented by (2) using the equivalent system swing equation.

$$2H_{sys} \frac{d\Delta\omega(t)}{dt} = P_{PFR,sys}(t) - P_d \quad (2)$$

where H_{sys} denotes the equivalent system inertia and $\Delta f(t)$ is system-wide frequency deviation. Substituting (1) into (2) yields a quadratic approximation of the frequency deviation, given by (3).

$$\frac{d\Delta\omega(t)}{dt} = \frac{P_d}{2H_{sys}} \left(\frac{t}{t_n} - 1 \right) \quad (3a)$$

$$\Delta\omega(t) = \frac{P_d}{2H_{sys}} \left(\frac{t^2}{2t_n} - t \right) \quad (3b)$$

While this simplification captures the general trend, it introduces significant inaccuracies due to the non-linear nature of turbine-governor responses. To improve accuracy, the PFR power of each

turbine-governor is formulated in the Laplace domain using the approximated frequency deviation, as

$$P_{PFR}(s) = (G \Delta\omega)(s) \quad (4)$$

where, $G(s)$ is the transfer function of the individual turbine-governor system. The Laplace-domain expressions of frequency deviation and PFR power, given by (3b) and (4), can be expressed as

$$\Delta\omega(s) = \frac{P_d}{2H_{sys}} \left(\frac{1}{t_n s^3} - \frac{1}{s^2} \right) \quad (5a)$$

$$P_{PFR}(s) = \frac{P_d}{2H_{sys}} \left(\frac{G(s)}{t_n s^3} - \frac{G(s)}{s^2} \right) \quad (5b)$$

Applying the inverse Laplace transform to (5b) yields the time-domain PFR responses, expressed as

$$P_{PFR}(t) = \frac{P_d}{2H_{sys}} \left(\frac{1}{t_n} z_2(t) - z_1(t) \right) \quad (6a)$$

$$P_{PFR,sys}(t) = \sum_{i=1}^N \alpha_i P_{PFR,i}(t) \quad (6b)$$

where α_i is the normalization coefficient, and z_n denotes the n -th integration of the unit step response (7) of the of each turbine-governor model.

$$z_n(t) = \mathcal{L}^{-1} \left\{ \frac{G(s)}{s^{n+1}} \right\} \quad (7)$$

This analytical expression allows the aggregated PFR, $P_{PFR,sys}$, to be represented using pre-simulated unit step responses of each turbine-governor model. Within this framework, t_n remains the only unknown, and the optimal t_n is determined by solving

$$t_n^* = \underset{t_n}{\operatorname{argmin}} |P_{PFR,sys}(t_n) - P_d| \quad (8)$$

A key advantage of this method is that the unit step response of each turbine-governor is system-specific and independent of power dispatch or network conditions. Consequently, the unit step responses need to be computed only once for each turbine-governor model and can be reused across different operating conditions, provided that the turbine-governor characteristics remain unchanged. This feature substantially reduces the computational burden in system dynamic studies.

III. DISCONTINUITY-AWARE FREQUENCY NADIR PREDICTION

A. Overall Methodology for DA-FNP model

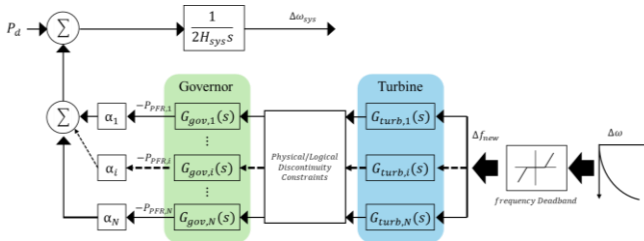


Fig. 2. Discontinuity-aware frequency nadir prediction (DA-FNP) model.

In this section, the analytical framework is extended to implement discontinuity constraints that limit turbine-governor

performance, as illustrated in Fig. 2. The discontinuities considered for the DA-FNP model include frequency deadband, physical constraints, and logical constraints, which are described as follows:

1) *Frequency deadband*: The frequency deadband is applied to avoid unnecessary governor actions caused by measurement noise and to prevent governor response within a specified range. While this improves stability against small fluctuations, it also delays the frequency restoration process after a disturbance. Analytically, it is expressed as

$$\Delta\omega_{new} = (\Delta\omega(t) - \Delta\omega_{db})u(t - t_{db}), t \in [0, t_n] \quad (9)$$

where t_{db} denotes the time when governor response begins, $\Delta\omega_{db}$ denotes deadband threshold, and $u(t)$ is the unit step function.

2) *Physical constraints*: Physical constraints represent inherent equipment limitations, such as valve position limits in governor systems. For example, the valve position is bounded by maximum and minimum limits, and these limits are reached, the signal remains constant. In block-diagram representations used in detailed dynamic simulations, such constraints are typically implemented using limiter blocks. Analytically, this can be expressed as

$$u_{input}(t) := \begin{cases} x(t), & t \in [0, t_{lim}) \\ x(t_{lim}), & t \in [t_{lim}, t_n) \end{cases} \quad (10)$$

$$y(t) = f(u_{input}(t))$$

where t_{lim} denotes the time when the constraint is violated, $x(t)$ denotes the input to constraints, and $y(t)$ is the output.

3) *Logical Constraints*: Logical constraints reflect supervisory control strategies designed to optimize performance and maintain stability. For instance, in gas turbines, the lowest valve position selector ensures coordination between multiple operating limits. Unlike physical constraints, logical constraints dynamically adjust the block diagram based on signal conditions in the detailed dynamic simulation. Analytically, this constraint is expressed as

$$u_{input}(t) := \begin{cases} x_1(t), & t \in [0, t_{lim}) \\ x_2(t), & t \in [t_{lim}, t_n) \end{cases} \quad (11)$$

$$x_2(t) = g(u_{input}(t))$$

$$y(t) = f(u_{input}(t))$$

where $x_1(t)$ and $x_2(t)$ denote the input signals to constraints.

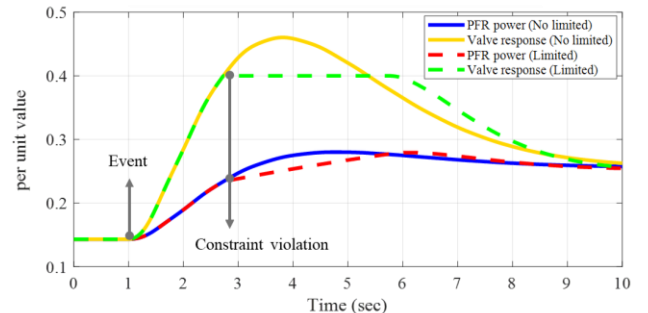


Fig. 3. Valve and PFR power response with/without constraints.

These discontinuity constraints substantially affect turbine–governor dynamics and, consequently, system frequency behavior. As an example, Fig. 3. Illustrates that physical constraints (e.g., valve position limits) restrict governor response, thereby reducing and delaying PFR power output. This alters the frequency trajectory, preventing it from exhibiting the characteristic parabolic profile typically approximated by a second-order polynomial.

One important consideration in limit-type discontinuities is the distinction between windup and non-windup limiters. In general, non-windup limiters allow the controller state to back off immediately once the saturation constraint is released, whereas windup limiters may retain the accumulated integrator state, resulting in delayed recovery behavior [27]. In this work, however, the proposed DA-FNP framework focuses exclusively on first-swing frequency dynamics, defined as the system response from the initial contingency to the frequency nadir. During this interval, the governor control error remains sign-consistent and drives the control action monotonically toward its bound. Consequently, the controller state does not reverse direction or back off from the limit prior to the nadir. As a result, the behavioral differences between windup and non-windup limiters do not influence the frequency trajectory up to the nadir. Therefore, the proposed method treats windup and non-windup limiters equivalently for first-swing frequency nadir prediction.

The core concept of implementing discontinuities is that, when the input is expressed as a polynomial function, the corresponding output can be approximated as a combination of the unit step response and its successive integrations at each stage of the turbine–governor model. These time-domain responses are pre-computed only once prior to prediction.

Assuming $f_{poly}(t)$ is an N -th order polynomial, the Laplace transforms of polynomial inputs multiplied by the unit step function for delayed activation, which is used extensively in this paper, can be expressed according to binomial theorem as follows

$$f_{poly}(t) = \sum_{n=0}^N a_n t^n$$

$$\mathcal{L}\{f_{poly}(t)u(t-\tau)\} = \sum_{n=0}^N \left[a_n n! \sum_{k=0}^n \frac{\tau^k}{k!} \frac{e^{-s\tau}}{s^{n-k+1}} \right]$$

Using these fundamental Laplace transforms for polynomial equation, the analytical time-domain outputs can be derived from the unit step response of the system.

For readability, we define the following function generator, which produces the time-domain representation as expressed in (12). The symbol # serves as a placeholder denoting the type of time-domain data used by each stage of turbine-governor model (feedback, turbine, governor, etc):

$$W_{\#}(t; \mathbf{a}, \tau) = \sum_{n=0}^{\dim(\mathbf{a})} \left[a_n n! \sum_{k=0}^n \frac{\tau^k}{k!} Z_{\#,n-k}(t-\tau) \right] \quad (12)$$

where $Z_{\#,n}(t)$ is the n -th integration of the unit step response of the of specific # system, defined as

$$Z_{\#,n}(t) = \mathcal{L}^{-1} \left\{ \frac{G_{\#}(s)}{s^{n+1}} \right\}$$

Therefore, the time-domain output of system #, when driven by a polynomial input with delayed activation through the function generator, can be expressed as

$$\begin{cases} Y(s) = G_{\#}(s) \mathcal{L}\{f_{poly}(t)u(t-\tau)\} \\ y(t) = W_{\#}(t; \mathbf{a}, \tau) \end{cases} \quad (13)$$

B. Frequency Deadband

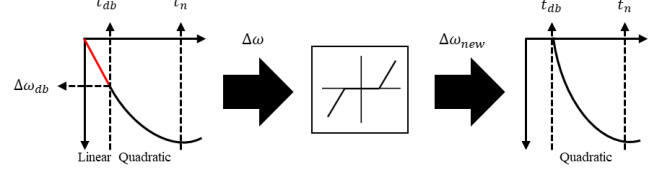


Fig. 4. Frequency deadband implementation for turbine-governor input.

Within the deadband threshold, the frequency response is filtered, as shown in Fig. 4. The system frequency response initially follows a linear trajectory with constant slope $(\frac{P_d}{2H_{sys}})$, until the deadband is reached, after which the response transitions to a quadratic trajectory. Accordingly, the frequency deviation can be expressed as

$$\Delta\omega(t) \approx (at^2 + bt + c)u(t - t_{db}) - \frac{P_d}{2H_{sys}} tu(t) \quad (14)$$

To determine the coefficients a , b , c , and deadband time t_{db} , continuity and differentiability conditions are imposed:

$$\begin{cases} \Delta\omega(t_{db}^-) = \Delta\omega(t_{db}^+) = \Delta\omega_{ab} \\ \Delta\omega'(t_{db}^+) = \Delta\omega'(t_{db}^-) = -\frac{P_d}{2H_{sys}} \\ \Delta\omega'(t_n) = 0 \end{cases}$$

From these conditions, the parameters are obtained as

$$t_{db} = \frac{|\Delta\omega_{ab}| 2H_{sys}}{P_d} \quad a = \frac{P_d}{4H_{sys}} \left(\frac{1}{t_n - t_{db}} \right)$$

$$b = -2at_{db} \quad c = at_{db}^2$$

Finally, by substituting (14) with specified parameters into (9), the frequency deviation after the deadband can be expressed as

$$\Delta\omega_{new}(t) \approx u(t - t_{db}) \sum_{n=0}^2 a_n t^n \quad (15)$$

with

$$\mathbf{a}^T = [c - \Delta\omega_{ab} \quad b - \frac{P_d}{2H_{sys}} \quad a]$$

Notably, when the deadband threshold $\Delta\omega_{ab}$ is zero, the constrained frequency response becomes identical to the frequency expression presented in Section 2.

C. Physical Discontinuity Constraints

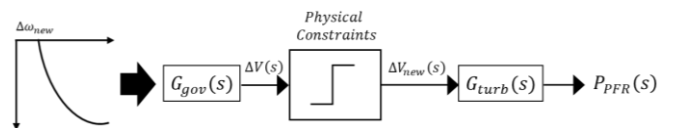


Fig. 5. DA-FNP model configuration with physical constraints.

To implement the physical constraints, the valve response is separated into the unconstrained and constrained cases according to before and after constraints, as shown in Fig. 5. The unconstrained valve response ΔV , is influenced by the frequency deadband and is obtained by passing the constrained frequency response $\Delta\omega_{new}$ through the governor transfer function G_{gov} :

$$\Delta V(s) = (G_{gov}\Delta\omega_{new})(s) \quad (16)$$

In the time domain, the response is represented as:

$$\Delta V(t) = W_{gov}(t; \mathbf{a}, t_{db}) \quad (17)$$

where $W_{gov}(t; \mathbf{a}, t_{db})$ is the function generator defined in (13), obtained by substituting (15) into (16). Based on (10), the constrained valve response ΔV_{new} , can be expressed as

$$\Delta V_{new}(t) = \begin{cases} \Delta V(t)u(t - t_{db}), & t \in [0, t_{lim}] \\ \Delta V(t_{lim}), & t \in [t_{lim}, t_n] \end{cases}$$

Accordingly, the constrained PFR power is formulated by passing the constrained valve response through the turbine transfer function G_{turb} :

$$P_{PFR}(s) = (G_{turb}(s)\Delta V_{new})(s) \quad (18)$$

This can be equivalently decomposed into the Laplace and time domain as

$$P_{PFR} = P_{PFR}^{(1)} + P_{PFR}^{(2)} + P_{PFR}^{(3)} \quad (19)$$

with Laplace domain definitions

$$P_{PFR}^{(1)}(s) := G_{turb}(s)\mathcal{L}\{\Delta V(t)u(t - t_{db})\}$$

$$P_{PFR}^{(2)}(s) := G_{turb}(s)\mathcal{L}\{-\Delta V(t)u(t - t_{lim})\}$$

$$P_{PFR}^{(3)}(s) := G_{turb}(s)\mathcal{L}\{\Delta V(t_{lim})u(t - t_{lim})\}$$

These terms represent the unconstrained response ($P_{PFR}^{(1)}$), the fade-out effect due to constraint enforcement ($P_{PFR}^{(2)}$), and the constant contribution after limit violation ($P_{PFR}^{(3)}$), respectively. To analytically represent the constrained PFR power as a combination of the unit step responses and their successive integrations, ΔV in (19) is approximated by an N -th order polynomial after t_{db} :

$$\Delta V(t) \approx u(t - t_{db}) \sum_{n=0}^N p_n t^n \quad (20)$$

where p_n are the fitted polynomial coefficients. Substituting (20) into (19) and applying the function generator in (13), the physically constrained PFR power in the time domain is obtained as the sum of the follows:

$$P_{PFR}^{(1)}(t) = W_{turb}(t; \mathbf{p}, t_{db})$$

$$P_{PFR}^{(2)}(t) = -W_{turb}(t; \mathbf{p}, t_{lim}) \quad (21)$$

$$P_{PFR}^{(3)}(t) = W_{turb}(t; \Delta V(t_{lim}), t_{lim})$$

D. Logical Discontinuity Constraints

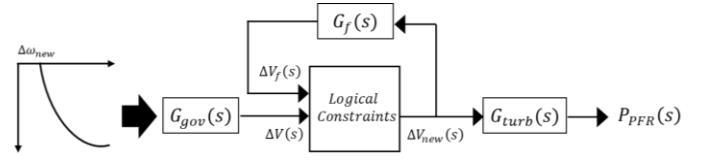


Fig. 6. DA-FNP model configuration with logical constraints.

Logical constraints modify the block diagram according to input signals, ensuring efficient implementation of control strategies. These signals, represented by the valve and feedback responses, are illustrated in Fig. 6.

Based on (11), the valve response under logical constraints is defined as

$$\Delta V_{new}(t) = \begin{cases} \Delta V(t)u(t - t_{db}), & t \in [0, t_{lim}] \\ \Delta V_f(t), & t \in [t_{lim}, t_n] \end{cases}$$

where the feedback-modified valve response is defined in the Laplace domain by passing the constrained valve response ΔV_{new} through the feedback transfer function G_f :

$$\Delta V_f(s) = (G_f\Delta V_{new})(s)$$

Analogous to the physical constraints case, the feedback valve response can be decomposed into three components as

$$\Delta V_f = \Delta V_f^{(1)} + \Delta V_f^{(2)} + \Delta V_f^{(3)}$$

with Laplace domain definitions

$$\Delta V_f^{(1)}(s) := G_f(s)\mathcal{L}\{\Delta V(t)u(t - t_{db})\}$$

$$\Delta V_f^{(2)}(s) := G_f(s)\mathcal{L}\{-\Delta V(t)u(t - t_{lim})\}$$

$$\Delta V_f^{(3)}(s) := G_f(s)\mathcal{L}\{\Delta V_f(t)u(t - t_{lim})\}$$

The first two terms can be expressed in the time domain using the function generator with polynomial expression for valve response in (20) and the unit step response of G_f .

$$\Delta V_f^{(1)}(t) = W_f(t; \mathbf{p}, t_{db})$$

$$\Delta V_f^{(2)}(t) = -W_f(t; \mathbf{p}, t_{lim})$$

To handle $\Delta V_f^{(3)}$, the input ΔV_f is split into known and unknown parts. The combined known response is approximated by a fitted polynomial as

$$(\Delta V_f^{(1)} + \Delta V_f^{(2)})(t) \approx u(t - t_{db}) \sum_{n=0}^N q_n t^n \quad (22a)$$

while the unknown component is expressed by polynomial with unknown coefficients as

$$\Delta V_f^{(3)}(t) \approx u(t - t_{lim}) \sum_{n=0}^N c_n t^n \quad (22b)$$

where, q_n is fitted polynomial coefficient and c_n is an unknown polynomial coefficient. Substituting (22) into the Laplace expression of $\Delta V_f^{(3)}$ gives an alternative form of time domain

TABLE I
COMPARISON OF FREQUENCY NADIR PREDICTION METHODS.

Modeling Type	Data-driven optimization		Online estimation		Analytical estimation		
Article	Y. Shen, et. al (2022) [25]	X. Liu, et. al, (2024) [26]	Z. Peng, et. al, (2024) [15]	D. Lekshmi J, et. al, (2024) [23]	L. Liu, et. al, (2020) [14]	Z. Zhao, et. al, (2025) [21]	Proposed DA-FNP
Data dependency	High (historical data)	High (UC data)	Medium (measurements)	High (measurements)	Low (model-based)	Low (model-based)	Low (model-based)
Governor model	Implicit/Simplified	Implicit	Explicit	Implicit	Explicit	Explicit	Explicit
IBR model	Not modeled	Implicit	Implicit	Implicit	Not modeled	Explicit	Extendable
Frequency trajectory	No	No	Yes	No	Yes	Yes	Yes
Discontinuity modeling	Not considered	Not considered	Not considered	Not considered	Not considered	Not considered	Explicit

recalculated using the discontinuity-aware formulations derived in Section III. The system-wide PFR in (26) is then updated as

$$P_{PFR,sys}(t) = \sum_{i \in UC} \alpha_i P_{UC,i}(t) + \sum_{i \in C} \alpha_i P_{C,i}(t)$$

where P_{UC} and P_C denote the unconstrained and constrained PFR power, respectively.

Step 4: The nadir time is updated using (27) with the updated $P_{PFR,sys}$. Steps 2–4 are repeated until the set of constrained generators remains unchanged between iterations.

Step 5: Once convergence is achieved, the system frequency trajectory is determined from the aggregated PFR power as

$$\frac{d\Delta\omega_{sys}(t)}{dt} = \frac{1}{2H_{sys}} (P_{PFR,sys}(t) - P_d)$$

V. CASE STUDY

Before presenting the case studies, Table I summarizes the key differences between the proposed DA-FNP framework and representative frequency nadir prediction approaches reported in the literature, including analytical, data-driven, and online-based methods. Existing approaches are typically designed for optimization or estimation purposes under smooth system assumptions, and therefore do not explicitly capture discontinuities. In contrast, the proposed DA-FNP framework explicitly incorporates physics- and control-induced discontinuities such as deadbands, physical, and logical constraints, while preserving the analytical tractability and scalability of low-order models.

The performance of DA-FNP model is validated by the Hawaii and Texas synthetic grids for small- and large-scale test cases, respectively. The synthetic grid cases can be accessed in [28] with a transmission network that is geo-located but is fictitious and does not correspond to any actual grid. A summary of case information is provided in Table II.

TABLE II
THE SUMMARY OF THE BASSE SYNTHETIC GRIDS
- Hawaii synthetic grid

Num. of Gen	Num. of buses	Generation [MW]	Load [MW]
30	37	1,154	1,136

- Texas synthetic grid

Num. of Gen	Num. of buses	Generation [MW]	Load [MW]
313	2,000	58,370	57,043

For comparison of the impact of each constraint, five different scenarios are created as follows:

- Scenario A: no discontinuity constraints present (all limits and frequency deadband removed),
- Scenario B: only frequency deadband present,
- Scenario C: only physical constraints present,
- Scenario D: only logical constraints present, and
- Scenario E: All discontinuity constraints present: both physical and logical constraints with deadband (original case).

The frequency deadband in Scenario B is set to ± 0.02 Hz for the governor response, based on industry recommendations provided by the North American Electric Reliability Corporation (NERC) [29]. The chosen value lies well within maximum allowable limits of industry, clearly differentiating between Scenario A and Scenario B.

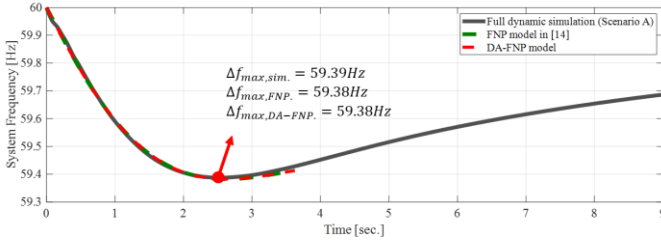
The DA-FNP model estimates the system frequency trajectory until it approaches the frequency nadir. The performance of the proposed model is confirmed by the relative error (RE) between maximum frequency deviation, Δf_{max} in full dynamic simulation (PowerWord) [30] and estimation.

$$RE [\%] = \frac{|\Delta f_{max, sim.} - \Delta f_{max, est.}|}{\Delta f_{max, est.}} \times 100$$

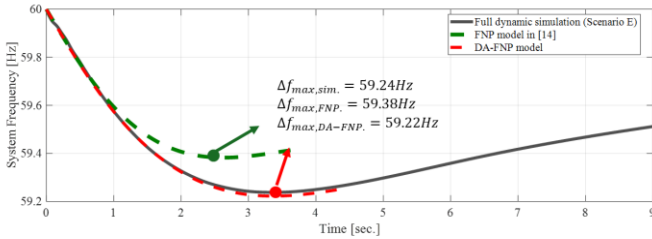
A. Hawaii Synthetic Grid: 37-Bus and 30-Generator

The Hawaii synthetic grid is used for validating the performance of the DA-FNP model in small-scale grid. Fig. 8 illustrates the system frequency response obtained from both the full dynamic simulation and the proposed model during two-generator outage event. The results show that the original FNP model fails to account for discontinuity characteristics, leading to inaccurate estimations of frequency behavior.

Fig. 8(a) demonstrates that both the original and proposed models accurately capture the frequency response under Scenario A, where no discontinuity constraints are present. Fig. 8(b) validates the effectiveness of the DA-FNP model in Scenario E, which incorporates both physical and logical constraint violations as well as the frequency deadband effect. In this case, the proposed model achieves a maximum frequency deviation error of 1.96% compared with the full dynamic simulation. A summary of all test scenarios is provided in Table III, including the frequency nadir, nadir time, number of generators violating each type of constraint, and the associated error relative to the full dynamic simulation.



(a) No discontinuity constraints test: Scenario A.



(b) Both physical and logical constraints with deadband test: Scenario E.

Fig. 8. System frequency response from the full dynamic simulation, FNP, and DA-FNP (Hawaii synthetic grids).

Fig. 9 demonstrates the DA-FNP model consistently maintains a maximum frequency deviation error below 2% across all scenarios and it shows improved performance compared to original model.

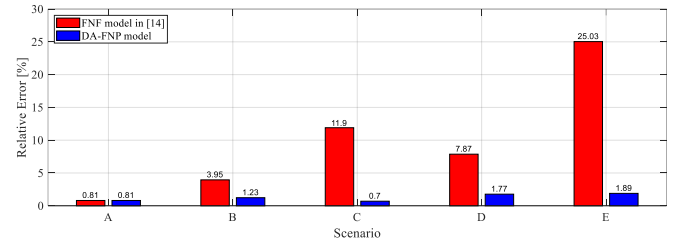


Fig. 9. The relative error of original and proposed FNP models to full dynamic simulation.

The proposed method is validated through a comparison of N-1 generator outage contingency results obtained from both full dynamic simulations and the DA-FNP model. Fig. 10 illustrates the maximum frequency deviation results from 30 scenarios of N-1 generator outage in the Hawaii synthetic grid, demonstrating reasonable differences across all contingencies.

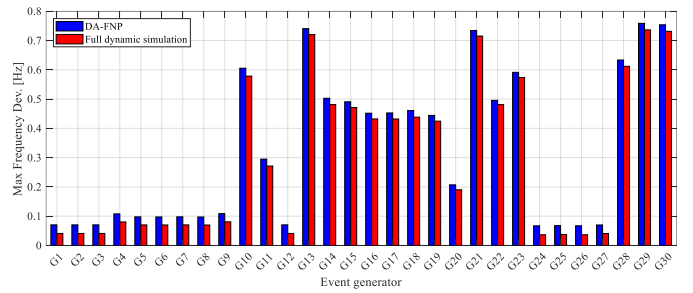


Fig. 10. Bar chart of maximum frequency deviation (Hawaii synthetic grids).

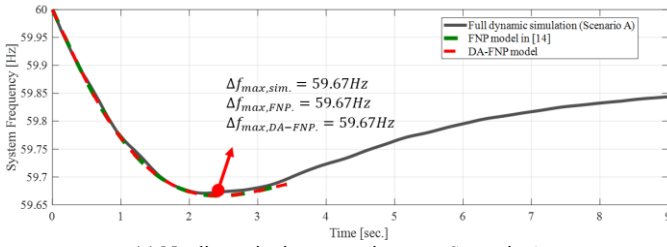
B. Texas Synthetic Grids: 2000-Bus and 313-Generator

To further assess the scalability of the DA-FNP model, the model is validated in the Texas synthetic case for large-scale grids. Fig. 11 presents the system frequency response under discontinuity characteristics during a two largest generators outage event. As shown in Fig. 11(a), both the original and proposed FNP models accurately capture the frequency response under Scenario A, representing ideal operating conditions without discontinuity constraints. Fig. 11(b) illustrates Scenario E, where both physical and logical constraints, with the frequency deadband effect, are considered.

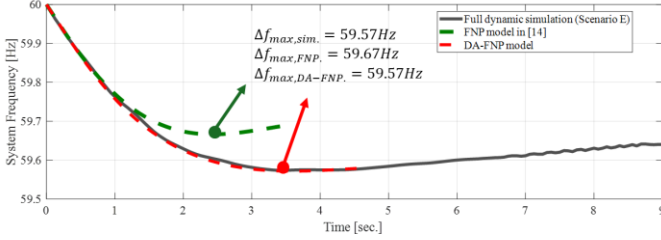
In this case, the proposed model achieves a maximum frequency deviation error of less than 0.5% compared to the full dynamic simulation. A summary of all test scenarios is provided in Table IV. Across all scenarios, the proposed model consistently maintains a relative error below 2.5%.

TABLE III
FREQUENCY NADIR PREDICTION RESULT ACROSS ALL SCENARIOS (HAWAII SYNTHETIC GRIDS)

Scenario	f_n [Hz]		t_n [sec.]		N_c		RE [%]
	Simulation	DA-FNP	Simulation	DA-FNP	Physical	Logical	
A	59.3874	59.3824	2.52	2.63	0	0	0.81
B	59.3580	59.3500	2.59	2.69	0	0	1.23
C	59.3089	59.3137	3.03	3.03	9	0	0.70
D	59.3338	59.3454	3.08	3.08	0	3	1.77
E	59.2376	59.2223	3.37	3.36	7	3	1.96

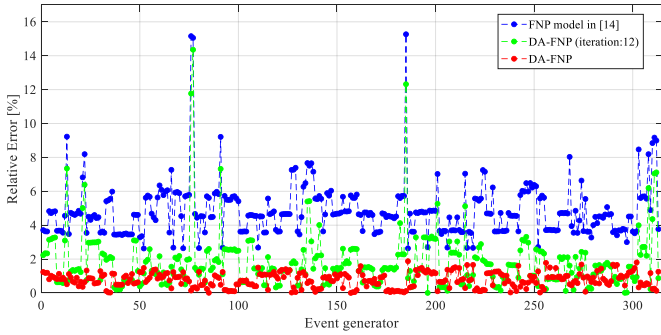


(a) No discontinuity constraints test: Scenario A.

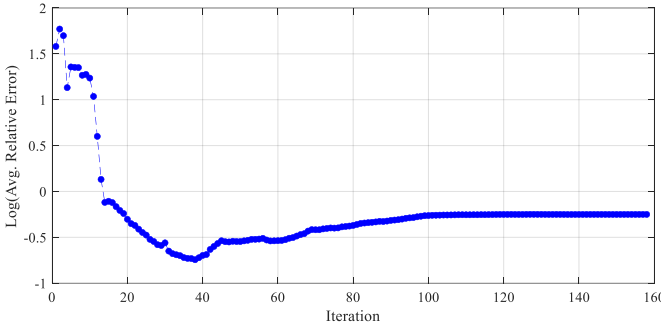


(b) Both physical and logical constraints with deadband test: Scenario E.

Fig. 11. System frequency response from the full dynamic simulation, FNP and DA-FNP (Texas synthetic grids).



(a) The relative error for each contingency.



(b) The average relative error at each iteration.

Fig. 12. The relative error of Δf_{max} compared between the full dynamic simulation and DA-FNP model.

Similar to the contingency test on the Hawaii synthetic grid, the proposed method is validated the Texas synthetic grid under Scenario E, encompassing 312 scenarios of N-1 generator outages occurring simultaneously with the largest generator outage. Fig. 12 illustrates the variation in relative error across iterations, comparing the proposed estimation method with the simulation results. As shown in Fig. 12(a), the relative error for every contingency is significantly reduced compared to the original FNP model, with errors remaining below 2% in every scenario. The iterative process in the DA-FNP model detects constraint violations at each iteration and updates the frequency nadir accordingly. By updating the frequency nadir and identifying generators that violate constraints, the proposed method enhances the accuracy of system frequency response estimation showing 0.77% of average relative error, as shown in Fig 12(b).

Table V summarizes the results of the contingency tests in the Texas synthetic grids with the highest error and the largest frequency deviation, validating the model's robustness in predicting system frequency response under practical operating conditions.

TABLE V
THE MAXIMUM FREQUENCY DEVIATION TEST-TEXAS CASE

Case: Texas	Event	Δf_{max} [Hz]		RE [%]
		Simulation	DA-FNP	
Highest error	G301	0.2076	0.2107	1.80
Largest deviation	G76	0.4265	0.4271	0.14

C. Contingency Scalability

While the case studies focus on N-1 generator outages, which are standard benchmarks in frequency stability analysis, the modeling framework is inherently generalizable and scalable to more complex disturbances. Multiple simultaneous contingencies or other events can be equivalently represented through their impact on the net active power balance, denoted as P_d . In the proposed DA-FNP framework, P_d is driven by the mismatch between mechanical power input, load demand, and system losses:

$$P_d = \Delta P_m - \Delta P_L - \Delta P_{loss},$$

where ΔP_m represents the change in mechanical power input, ΔP_L denotes the change in load demand, and ΔP_{loss} accounts for

TABLE IV
FREQUENCY NADIR PREDICTION RESULT ACROSS ALL SCENARIOS (TEXAS SYNTHETIC GRIDS)

Scenario	f_n [Hz]		t_n [sec.]		N_c		RE [%]
	Simulation	DA-FNP	Simulation	DA-FNP	Physical	Logical	
A	59.6709	59.6663	2.25	2.43	0	0	1.38
B	59.6427	59.6343	2.31	2.54	0	0	2.3
C	59.6329	59.6338	2.88	2.73	29	0	0.25
D	59.6490	59.6498	3.13	2.86	0	211	0.23
E	59.5736	59.5716	3.44	3.59	29	220	0.47

variations in system losses after events. Any contingency that can be expressed as an effective change in P_d can be directly incorporated into the DA-FNP framework without modifying the formulation, highlighting the generality and scalability of the approach.

D. Computational Efficiency

The proposed method is computationally fast, both in asymptotic analysis and in practice. The execution time of a full dynamic simulation to obtain the frequency nadir is characterized by $\gamma \in [0.2, 0.5]$, a sparse system parameter as discussed in [31]. The time-per-iteration parameter α is system dependent.

$$T(n) = \left(\frac{\alpha t_n}{\Delta t}\right) n^{1+\gamma} = O(n^{1+\gamma})$$

The execution time of proposed method is characterized by T_f and $\beta \in [0, 1]$ which denote the polynomial fitting computation time and the percentage of generators that observe a violation, respectively.

$$T'(n) = 2\beta T_f n = O(n)$$

The theoretical relative efficiency of the proposed method is measured by the ratio of execution times.

$$\eta = \frac{T(n)}{T'(n)} = \left(\frac{n^\gamma}{2\beta}\right) \frac{\alpha t_n}{T_f \Delta t} = O(n^\gamma)$$

Thus, the computational speedup is expected to grow with the number of generators, and can be bounded as follows.

$$O(n^{0.2}) \leq \eta \leq O(n^{0.5})$$

Table VI illustrates the computation times observed for the proposed method in practice, relative to a commercial full dynamic simulation tool (PowerWorld) on the same machine. The N-1 generator outage contingency tests are performed, and the results show the proposed method has a total speedup of 29x for the synthetic Hawaii case and 146x for the synthetic Texas case.

TABLE VI
COMPUTATION TIME RESULTS

Computation Time [s]	Hawaii ($\beta_{avg}=0.19$)		Texas ($\beta_{avg}=0.05$)	
	Simulation	DA-FNP	Simulation	DA-FNP
Total of all contingencies	10.17	0.35	949.01	6.51
Average contingency	0.34	0.01	3.03	0.02
Worst-case contingency	0.38	0.05	4.53	0.5

Based solely on the difference in the number of generators, the theoretical efficiency enhancement from the Hawaii to the Texas case is expected to range between 1.6x and 3.2x, while the practical improvement is approximately 5x, exceeding the theoretical estimate that assumes other factors, such as system sparsity, the fraction of violated generators, and solver overhead, remain equal. Overall, the empirical results are

consistent with the predicted asymptotic scaling behavior with additional improvement influenced by system-dependent effects, indicating that the DA-FNP framework maintains efficient and scalable performance for larger systems.

VI. CONCLUSION

This paper proposes a newly formulated discontinuity-aware frequency nadir prediction (DA-FNP) model that explicitly implements discontinuity constraints including frequency deadbands, physical constraints, and logical constraints into system frequency response estimation. By incorporating these practical features, the proposed framework overcomes limitation of existing low-order models, which often fail to reproduce the fidelity of detailed dynamic simulations.

The effectiveness and scalability of the DA-FNP model are demonstrated through case studies on the Hawaii (37-bus, 30-generator) and Texas (2000-bus, 313-generator) synthetic grids. Across both systems, the model achieved significant improvements in predicting frequency nadir and overall frequency trajectory compared to the original FNP formulation. To systematically assess the influence of each discontinuity, five representative scenarios (A–E) were evaluated. The proposed approach consistently maintained less than 3% relative error across all scenarios and test systems, while the original FNP model was accurate only under Scenario A and produced substantially higher errors otherwise. Furthermore, N-1 contingency analyses confirmed the robustness of the proposed method across diverse operating conditions. At the same time, the model preserved the computational efficiency of a reduced-order formulation, yielding speedups of 29x for the synthetic Hawaii grid and 146x for the synthetic Texas grid.

The proposed DA-FNP framework focuses on discontinuity-aware modeling of governor-based frequency response; however, its underlying formulation is general and not restricted to synchronous generators. The framework is constructed around a frequency deviation to active power response structure, which is equally applicable to inverter-based resources. Reduced-order models for both grid-following (GFL) and grid-forming (GFM) inverters reported in the literatures [15], [21] represent inverter active power injection as an explicit function of frequency deviation. By integrating such reduced-order inverter models into the DA-FNP formulation, control-induced discontinuities inherent to inverter controls, including saturation limits, droop control, and virtual inertia constraints, can be analytically incorporated using the same discontinuity-handling logic developed in this work. The proposed methodology, therefore, can be naturally extended to systems with varying levels of renewable penetration by augmenting the set of frequency-dependent power injection elements representing a variety of frequency regulation resources around power systems, without modifying the fundamental structure of the DA-FNP model. A comprehensive quantitative assessment of mixed GFM and GFL inverter systems under different renewable penetration levels is identified as an important direction for future work.

Overall, the DA-FNP model provides a practical and scalable tool for power system planning studies. By enabling

more reliable assessment of frequency security margins and resource adequacy, the framework provides system operators and planners with enhanced capability to ensure stability in modern power grids.

APPENDIX A

Equation (23) can be simplified and expressed in a linearized matrix form:

$$A_1 \mathbf{c} = A_2 (\mathbf{q} + \mathbf{c})$$

with:

- the n -th column of $A_1 := t^n u(t - t_{lim})$, and A_1 is a matrix of (*length of time* $\times N$), representing the time evolution with a time-shift, t_{lim} ,
- the n -th column of $A_2 := n! \sum_{k=0}^n \left(\frac{t_{lim}^k}{k!} Z_{f,n-k}(t - t_{lim}) \right)$, and A_2 is a matrix of (*length of time* $\times N$), representing the integrations of unit step response with a time-shift, and
- the n -th element of $\mathbf{c} := c_n$, and \mathbf{c} is a $N \times 1$ vector, representing the unknown coefficients of the polynomial equation.

The optimal polynomial coefficient vector, \mathbf{c}^* is derived using the least squared error optimization:

$$\mathbf{c}^* = \underset{\mathbf{c}}{\operatorname{argmin}} \|(A_1 - A_2)\mathbf{c} - A_2\mathbf{q}\|_2$$

or

$$\mathbf{c}^* = (A_1 - A_2)^+ A_2 \mathbf{q}$$

REFERENCES

- [1] Electric Reliability Council of Texas (ERCOT), "Inertia: Basic Concepts and Impacts on the ERCOT Grid," White paper, April 2018.
- [2] North American Electric Reliability Corporation (NERC), "Fast Frequency Response Concepts and Bulk Power System Reliability Needs," White paper, Mar 2020.
- [3] North American Electric Reliability Corporation (NERC), "Automatic Underfrequency Load Shedding," Std. PRC-006-2, Nov. 2014.
- [4] Electric Reliability Council of Texas (ERCOT), "Load Shed Protocols for ERCOT Region," White paper, Aug. 2022.
- [5] Federal Energy Regulatory Commission (FERC), North American Electric Reliability Corporation (NERC), and Regional Entities, "The February 2021 Cold Weather Outages in Texas and the South Central United States," Staff Report, Nov. 2021.
- [6] Australian Energy Market Operator (AEMO), "Black System South Australia 28 September 2016," Mar. 2017.
- [7] M. L. Chan, R. D. Dunlop and F. Schweppe, "Dynamic Equivalents for Average System Frequency Behavior Following Major Disturbances," in IEEE Trans. on Power Apparatus and Systems, vol. PAS-91, no. 4, pp. 1637-1642, July 1972.
- [8] P. M. Anderson and M. Mirheydar, "A low-order system frequency response model," in IEEE Trans. on Power Syst., vol. 5, no. 3, pp. 720-729, Aug. 1990.
- [9] M. Niu, G. Zhang, Y. Ren and J. Li, "An Analytical Model for Frequency Nadir Prediction Based on Probabilistic Production Simulation," 2022 IEEE 5th International Conference on Automation, Electronics and Electrical Engineering (AUTEEE), Shenyang, China, 2022, pp. 89-95.
- [10] B. Wang et al., "Sparse Measurement-Based Modelling Low-Order Dynamics for Primary Frequency Regulation," in IEEE Trans. on Power Syst., vol. 39, no. 1, pp. 681-692, Jan. 2024.
- [11] Z. Zhao, K. Zhang, Y. Xue, Z. Li, Y. Tang and Z. Wu, "Generic Low-Order Primary Frequency Response Model for Frequency Nadir Prediction," 2024 China International Conference on Electricity Distribution (CICED), Hangzhou, China, 2024, pp. 946-952.
- [12] Y. Cao, H. Zhang, Y. Zhang, Y. Xie, and C. Ma, "Extending SFR model to incorporate the influence of thermal states on primary frequency response," IET Gener. Transm. Distrib., vol. 14, issue 19, pp. 4069-4078, June 2020.
- [13] I. Egido, F. Fernandez-Bernal, P. Centeno and L. Rouco, "Maximum Frequency Deviation Calculation in Small Isolated Power Systems," in IEEE Trans. on Power Syst., vol. 24, no. 4, pp. 1731-1738, Nov. 2009.
- [14] L. Liu, W. Li, Y. Ba, J. Shen, C. Jin and K. Wen, "An Analytical Model for Frequency Nadir Prediction Following a Major Disturbance," in IEEE Trans. on Power Syst., vol. 35, no. 4, pp. 2527-2536, July 2020.
- [15] Z. Peng, Q. Peng, Y. Zhang, H. Han, Y. Yin and T. Liu, "Online Inertia Allocation for Grid-Connected Renewable Energy Systems Based on Generic ASF Model Under Frequency Nadir Constraint," in IEEE Trans. on Power Syst., vol. 39, no. 1, pp. 1615-1627, Jan. 2024.
- [16] D. A. Leiva Roca, P. Mercado and G. Suvire, "System Frequency Response Model Considering the Influence of Power System Stabilizers," in IEEE Latin America Trans., vol. 20, no. 6, pp. 912-920, June 2022.
- [17] D. L. H. Aik, "A general-order system frequency response model incorporating load shedding: analytic modeling and applications," in IEEE Trans. on Power Syst., vol. 21, no. 2, pp. 709-717, May 2006.
- [18] C. Fan, X. Wang, Y. Teng, and W. Wu, "Minimum frequency estimation of power system considering governor deadbands," IET Gener. Transm. Distrib., vol. 11, no. 15, pp. 3814-3822, Sep. 2017.
- [19] Y. Hu, Z. Wang, T. Huang, and Q. Zeng, "A novel frequency response analysis model applicable to high-penetration wind power grid," Energy Reports, vol. 8, pp. 412-421, 2022.
- [20] Z. Zhang, P. Kou, Y. Zhang, and D. Liang, "Coordinated predictive control of offshore DC collection grid and wind turbines for frequency response: A scheme without secondary frequency drop," IEEE Trans. Sustain. Energy, vol. 14, no. 3, pp. 1488-1503, Jul. 2023.
- [21] Z. Zhao, et al., "Generic Low-Order Primary Frequency Response Model for Frequency Nadir Prediction," in IEEE Transactions on Power Systems, vol. 40, no. 6, pp. 5221-5236, Nov. 2025.
- [22] N. Lu, "An Artificial Neural Network-Based Frequency Nadir Estimation Approach for Distributed Virtual Inertia Control," 2019 IEEE 4th International Future Energy Electronics Conference (IFEEC), Singapore, 2019, pp. 1-8.
- [23] D. Lekshmi J, Z. H. Rather and B. C. Pal, "Online Estimation of Disturbance Size and Frequency Nadir Prediction in Renewable Energy Integrated Power Systems," in IEEE Trans. on Power Syst., vol. 39, no. 1, pp. 1126-1137, Jan. 2024.
- [24] D. Zografos, T. Rabuzin, M. Ghandhari and R. Eriksson, "Prediction of Frequency Nadir by Employing a Neural Network Approach," 2018 IEEE PES Innovative Smart Grid Technologies Conference Europe (ISGT-Europe), Sarajevo, Bosnia and Herzegovina, 2018, pp. 1-6.
- [25] Y. Shen, et al., "Data-driven convexification for frequency nadir constraint of unit commitment," J. Mod. Power Syst. Clean Energy, vol. 11, pp. 1-7, Jan. 2022.
- [26] X. Liu, et al., "Frequency Nadir Constrained Unit Commitment for High Renewable Penetration Island Power Systems," in IEEE Open Access Journal of Power and Energy, vol. 11, pp. 141-153, 2024.
- [27] "IEEE Recommended Practice for Excitation System Models for Power System Stability Studies," in IEEE Std 421.5-2016 (Revision of IEEE Std 421.5-2005), pp. 1-207, 26 Aug. 2016.
- [28] "Electric Grid Test Case Repository". [Online]. Available: <https://electric.grids.engr.tamu.edu/>
- [29] North American Electric Reliability Corporation (NERC), "Primary Frequency Control Reliability Guideline," Sep. 2020.
- [30] PowerWorld Corporation. [Online]. Available: <http://www.powerworld.com/>
- [31] F. L. Alvarado, "Computational complexity in power systems," in IEEE Trans on Power App. and Syst., vol. 95, no. 4, pp. 1028-1037, July 1976.